Received: 3 January 2024 | Revised: 3 June 2024 | Accepted: 24 June 2024

DOI: 10.1002/mrm.30218

RESEARCH ARTICLE

Magnetic Resonance in Medicine

Phase stabilization with motion compensated diffusion weighted imaging

Ariel J. Hannum[1,2,3] | **Tyler E. Cork**[1,2,3] | **Kawin Setsompop**[1,4] | **Daniel B. Ennis**[1,2]

[1]Department of Radiology, Stanford University, Stanford, California, USA

[2]Division of Radiology, Veterans Administration Health Care System, Palo Alto, California, USA

[3]Department of Bioengineering, Stanford University, Stanford, California, USA

[4]Department of Electrical Engineering, Stanford University, Stanford, California, USA

Correspondence
Ariel J. Hannum, Department of Radiology, Stanford University, 1201 Welch Road, Stanford, CA 94305, USA.
Email: ahannum@stanford.edu

Funding information
National Institute of Health, Grant/Award Number: R01-HL152256; American Heart Association, Grant/Award Number: 23PRE1018442; National Science Foundation Graduate Research Fellowship Program, Grant/Award Number: DGE-1656518; National Science Foundation, Grant/Award Number: SCH-2205103

Abstract

Purpose: Diffusion encoding gradient waveforms can impart *intra-voxel* and *inter-voxel* dephasing owing to bulk motion, limiting achievable signal-to-noise and complicating multishot acquisitions. In this study, we characterize improvements in phase consistency via gradient moment nulling of diffusion encoding waveforms.

Methods: Healthy volunteers received neuro ($N = 10$) and cardiac ($N = 10$) MRI. Three gradient moment nulling levels were evaluated: compensation for position (M_0), position + velocity (M_1), and position + velocity + acceleration ($M_1 + M_2$). Three experiments were completed: (Exp-1) Fixed Trigger Delay Neuro DWI; (Exp-2) Mixed Trigger Delay Neuro DWI; and (Exp-3) Fixed Trigger Delay Cardiac DWI. Significant differences ($p < 0.05$) of the temporal phase SD between repeated acquisitions and the spatial phase gradient across a given image were assessed.

Results: M_0 moment nulling was a reference for all measures. In Exp-1, temporal phase SD for G_z diffusion encoding was significantly reduced with M_1 (35% of t-tests) and $M_1 + M_2$ (68% of t-tests). The spatial phase gradient was reduced in 23% of t-tests for M_1 and 2% of cases for $M_1 + M_2$. In Exp-2, temporal phase SD significantly decreased with $M_1 + M_2$ gradient moment nulling only for G_z (83% of t-tests), but spatial phase gradient significantly decreased with only M_1 (50% of t-tests). In Exp-3, $M_1 + M_2$ gradient moment nulling significantly reduced temporal phase SD and spatial phase gradients (100% of t-tests), resulting in less signal attenuation and more accurate ADCs.

Conclusion: We characterized gradient moment nulling phase consistency for DWI. Using M_1 for neuroimaging and $M_1 + M_2$ for cardiac imaging minimized temporal phase SDs and spatial phase gradients.

KEYWORDS

brain, cardiac, diffusion-weighted imaging, motion-compensation, phase

1 | INTRODUCTION

Diffusion-weighted MRI (DWI) probes the microstructural organization of soft tissues without the use of an exogenous contrast agent.[1,2] Diffusion is typically encoded via a spin-echo sequence, in which large monopolar gradients provide sensitivity to the thermally driven Brownian motion of water molecules. This results in a signal attenuation proportional to the magnitude of diffusion along the direction of the applied diffusion encoding gradient.[3] Differences in the measured apparent diffusion coefficient (ADC)[4] have clinical utility throughout the body, including detecting neurodegenerative disease,[5] determining malignant and benign liver lesions,[6,7] assessing breast lesions,[8,9] and more recently measuring fibrosis in the myocardium.[10]

Conventional diffusion encoding gradient waveforms primarily capture the self-diffusion of water molecules, resulting in the intended diffusion-weighted signal attenuation due to Brownian motion-induced *intra-voxel* phase dispersion. However, bulk tissue displacements[11,12] also introduce coherent *inter-voxel* phase shifts.[13,14] These phase shifts can be inconsistent between multiple shots (or averages), which complicates multishot acquisitions[15,16] and leads to signal dropouts. Furthermore, tissue deformation[17,18] introduces several *intra-voxel* signal artifacts[19] including nonlinear phase corruptions.[20] Notably, tissue deformation causes intra-voxel dephasing and additional signal attenuation that artificially increases apparent diffusion rates.[21]

Intra-voxel and *inter-voxel* phase discrepancies subsequently affect the temporal phase variation and spatial phase gradient of DWI acquisitions. Temporal phase variation can be defined as the phase difference between repeated acquisitions, whether it is sampling the image over multiple shots or acquiring many averages. *Intra-voxel* and *inter-voxel* phase differences for a given voxel decrease the fidelity of combining repeated acquisitions. Naively combining these averages or shots results in inaccurate signal representation for a given voxel.[22] The spatial phase gradient describes how the phase varies across a given two-dimensional image. Bulk motion can induce a linear phase across an image while changes in intra-voxel phase dispersion between adjacent voxels results in rapidly changing, noise-like phase.[23] These combined effects result in large spatial phase variations across the image, which make it harder to estimate and remove background phase.[22] Differences in the spatial phase gradient between repeated acquisitions or multiple shots increase the challenge of combining repeated acquisitions.

Multi-average and multishot DWI are limited by sensitivity to these temporal phase variations and spatial phase gradients. Single-shot echo-planar imaging (EPI) acquisitions in body DWI typically acquire multiple averages per acquisition to increase signal-noise-ratio (SNR); however, physiological motions on short time-scales are encoded into the phase that result in shot-to-shot phase inconsistencies and subsequent signal dropouts in averaged data.[24–26] Phase-encode[27–29] and readout-segmented[30,31] multishot acquisitions increase SNR and reduce blurring. Nonetheless, they can be compromised by a lack of phase stabilization. Motion-induced phase differences arising from both respiratory and cardiac-induced motion[32–34] can limit multishot neuroimaging resolution, and can be particularly problematic in multishot chest and abdominal applications.[35]

Diffusion encoding gradient waveforms with gradient moment nulling limit the sensitivity to intra-voxel velocity ($M_1 = 0$) and acceleration ($M_2 = 0$).[36] Velocity compensation (M_1) is utilized in body MRI applications such as the liver[37] and renal imaging.[38] Velocity and acceleration ($M_1 + M_2$) motion-compensated diffusion encoding gradient waveforms are the standard in cardiac DWI to mitigate signal losses due to larger bulk motions and tissue deformations.[39,40] However, the improvement of shot-to-shot phase consistency when using motion-compensated diffusion encoding gradients has yet to be investigated. If motion-compensated gradient waveforms minimize temporal phase differences and spatial phase gradients, then motion-compensated gradient waveforms may be a solution to enabling multishot DWI. The effects of gradient moment nulling for diffusion encoding on temporal phase variations and spatial phase gradients have also not been thoroughly investigated.

The objective of this work was to characterize the effectiveness of motion compensated diffusion encoding gradient waveforms for minimizing temporal phase variation and spatial phase gradients. We evaluated three different levels of gradient moment nulling in three different experiments in the brain and the heart.

2 | METHODS

2.1 | Experimental design

We conducted three different experiments to assess the *temporal* phase variations (σ_ϕ) and *spatial* phase gradients ($\mu_{||\phi||}$) of different diffusion encoding gradient moment nulling approaches: (1) no gradient moment nulling (M_0), (2) velocity compensation (M_1), and (3) velocity + acceleration compensation ($M_1 + M_2$) (Figure S1). For each measurement, one nondiffusion weighted image ($b = 0$) and three diffusion weighted images with diffusion-encoding along the scanner X, Y, and Z coordinates (G_x, G_y, and G_z) were acquired. Five repetitions were acquired for each

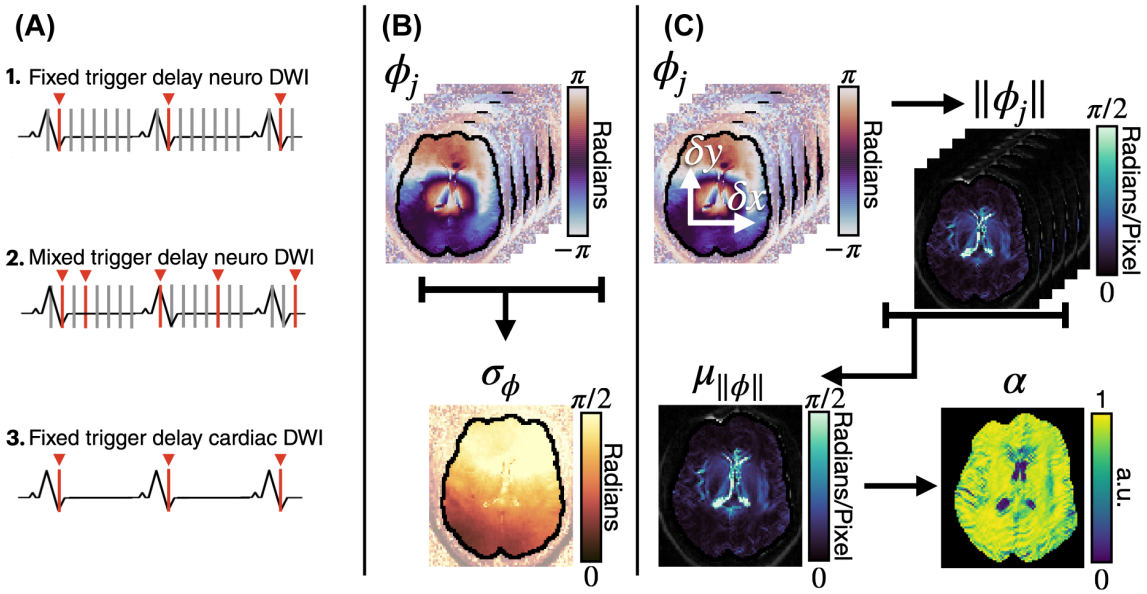

FIGURE 1 (A) Temporal phase SD and the spatial phase gradient were assessed in three experiments: (1) Neuro DWI images were acquired at a fixed trigger delay time (TD); (2) Neuro DWI were acquired at mixed TDs; and (3) Cardiac DWI were acquired at a fixed TD. (B) The pixel-to-pixel temporal phase SD, σ_ϕ, was computed between five repeated acquisitions. (C) The inter-voxel spatial phase gradient was computed pixel-wise and then the average spatial phase gradient, $\mu_{||\phi||}$, was then used to compute the attenuation coefficient (α), the amount of signal loss resulting from the spatial phase gradient. (A) Experiments; (B) Temporal; (C) Spatial.

trigger delay (TD) time. These experiments are outlined below and summarized in Figure 1.

2.1.1 | Experiment-1: fixed trigger delay Neuro DWI

We first assessed the effectiveness of gradient moment nulling (M_1 and $M_1 + M_2$) on phase consistency for neuroimaging when physiologic motion was also mitigated with ECG-gating. Brain DWI images were acquired at eight different TDs to assess temporal phase SD (σ_ϕ) and the spatial phase gradient ($\mu_{||\phi||}$) for a fixed TD of a given diffusion direction and slice position.

2.1.2 | Experiment-2: mixed trigger delay Neuro DWI

Phase consistency was then assessed between a random mixture of TDs for each form of gradient moment nulling. This mimicked a more conventional neuro DWI protocol acquired without ECG triggering. Experiment-1 images were pooled across all eight TDs and five averages. These forty images were then bootstrapped[41] 1000 times to generate individual datasets that each contained five images. This was performed for each moment nulling, slice, diffusion direction, and volunteer. Then for each dataset, the temporal phase SD σ_ϕ and the average spatial phase gradient $\mu_{||\phi||}$ were calculated to generate 1000 maps of each metric. The pixel-wise median and 95% confidence interval across the 1000 bootstraps were then computed for the temporal phase variation (σ_ϕ and $d\sigma_\phi$) and spatial phase gradients ($\mu_{||\phi||}$ and $d\mu_{||\phi||}$) to evaluate differences between levels of moment nulling.

2.1.3 | Experiment-3: fixed trigger delay cardiac DWI

Cardiac DWI was repeatedly acquired at a single TD (mid-systole) to evaluate phase consistency. Multiple TDs were not evaluated because of the lengthy exam time needed to do so thoroughly and owing to the limited range of TDs for which cardiac DWI is known to work well.[42,43] Temporal phase SD and spatial phase gradient were evaluated for this TD for a given diffusion direction and slice for a volunteer.

2.2 | Image acquisition

All imaging was completed on a 3T MRI system (Skyra, Siemens). For neuroimaging data, 10 volunteers ($N = 10$) were IRB consented and imaged using an, ECG-gated, single-shot EPI, spin-echo DWI sequence. Six slices were acquired with interleaved slice ordering and slice

TABLE 1 Image acquisition parameters.

Parameters	Neuro	Cardiac
Volunteers	$N = 10$ 27.0±5.7 years	$N = 10$ 26.7 ± 5.7 years
Coil	20-channel head	18-channel body 12-channel spine
Matrix Size	128 × 128	128 × 100
Slices	6 axial	3 short-axis
TE M_0 (ms)	73	47
TE M_1 (ms)	106	75
TE $M_1 + M_2$ (ms)	144	82
TR (ms)	3 × RR	3 × RR
Resolution (mm^3)	2 × 2 × 3	2 × 2 × 8
b-values (s/mm^2)	1000	250
Diffusion directions	G_x, G_y, G_z, $b = 0$	G_x, G_y, G_z, $b = 0$
Acceleration	GRAPPA 2	GRAPPA 2
Partial fourier	6/8	6/8
Bandwidth (Hz/Px)	1776	1776
Echo-spacing (ms)	0.68	0.68

coverage from the lower brainstem to the superior cortex (1 minute per slice). Each level of moment nulling was repeated for eight TDs that were determined by dividing the average R-R interval into 10 TDs and imaging the first eight TD. The 180° refocusing pulses of the different motion-compensated gradient waveforms were aligned[44] at each TD by applying a discrete offset to each TD for M_1 (19 ms) and M_0 (35.5 ms). For cardiac DWI, in a separate study, 10 volunteers ($N = 10$) were IRB consented and imaged with a free-breathing, ECG-gated, and respiratory-triggered, single-shot EPI spin-echo DWI sequence to acquire three short-axis slices (basal, mid-ventricular, and apical; 1 min per slice). Images were acquired at a single mid-systolic cardiac TD time. The TD was determined by running a trigger delay DWI scout with $M_1 + M2$ moment nulling for a mid-ventricular slice with diffusion encoding equal along the three orthogonal axis, while varying the trigger delay.[43] The TD with the highest signal coherency was then used with the corresponding M_1 and $M_1 + M_2$ timing offset. In this case, the 180° refocusing pulses for different levels of moment nulling were aligned by offsetting M_1 and M_0 by 3.5 and 17.5 ms, respectively. Complete imaging parameters are in Table 1.

2.3 | Postprocessing

All images were processed in Python (v3.8.8) with scripts from the Cardiac Diffusion in Python toolbox (CarDpy). The magnitude images were registered between TDs and repetitions using rigid registration for brain images, and affine registration for the cardiac images using the DiPy registration packages.[45] The registration transformation was then applied to both the real and imaginary components of the complex image data. Postregistration, brain images were masked via the Brain Extraction Tool[46] and the Medical Imaging Interaction Toolkit.[47] Cardiac images were masked with Medical Imaging Interaction Toolkit. Prior to phase evaluation, the mean $b = 0$ signal was complex subtracted from individual images to correct background phase sources (nonphysiological, eddy-current, etc.).

2.4 | Phase consistency evaluation

2.4.1 | Temporal phase SD

Temporal phase SD was used to assess pixel-wise phase variation between repeated single-shot acquisitions. To compute the temporal phase SD, the average phase (ϕ_{avg}) for a TD was first computed pixel-wise:

$$\phi_{\text{avg}} = \measuredangle \frac{1}{N} \sum_{j=1}^{j=N} \exp[-i\phi_j], \tag{1}$$

where j represents one repetition and N the total repetitions. Therefore, ϕ_j represents the pixel-wise phase of one image repetition. The difference phase ($\Delta\phi$) was then

computed between a given repetition and the ϕ_{avg} for a given TD on a pixel-wise basis:

$$\Delta\phi_j = \measuredangle \frac{\exp[-i\phi_j]}{\exp[-i\phi_{\text{avg}}]}. \tag{2}$$

This pixel-wise difference phase was then used to find the pixel-wise SD of the temporal phase (σ_r):

$$\sigma_\phi = \sqrt{\frac{\sum_{j=1}^{j=N}[\Delta\phi_j]^2}{N}}. \tag{3}$$

This pixel-wise phase SD map (σ_ϕ) was then computed for a given diffusion direction, slice, and repetition for each volunteer. The average (mean$\pm\sigma$) across a pixel-wise map was then computed to then make comparisons across gradient moment nulling levels.

2.4.2 | Spatial phase gradient

The spatial phase gradient was evaluated to characterize phase differences across pixels within a given repetition image. The magnitude of the spatial phase gradient ($\|\phi_i\|$) was computed for a given repetition at each TD:

$$\|\phi_j\|_{x,y} = \sqrt{\delta\phi_x^2 + \delta\phi_y^2}, \tag{4}$$

where $\delta\phi_x$ and $\delta\phi_y$ are pixel-wise spatial phase differences along the width and height of the image. Phase wrapping errors were corrected for by plotting the distribution of $\delta\phi_x$ or $\delta\phi_y$ pixels in a histogram with 20 evenly spaced bins from $-\pi$ to π. This histogram was fit with a kernel density plot distribution. If there was a local discontinuity in the distribution detected between $(-\pi, 0)$ or $(0, \pi)$, then pixels exceeding these local phase discontinuities would be indicative of phase wrapping. These values were corrected by adding or subtracting π. The pixel-wise mean ($\mu_{\|\phi\|}$) of the spatial phase gradient between five repetitions was evaluated (mean$\pm\sigma$). The mean across the masked spatial phase gradient image was then computed to evaluate differences for a given volunteer, slice and TD to assess different levels of gradient moment nulling.

2.4.3 | Signal attenuation ratio

The pixel-wise mean spatial phase gradient ($\mu_{||\phi||}$) was then used to calculate the signal attenuation ratio[48,49] (α) map in order to relate the phase distribution to resultant signal losses:

$$\alpha = \left| sinc\left(\mu_{||\phi||}\frac{r_x r_y}{2}\right)\right|, \tag{5}$$

where r_x and r_y are the in-plane resolution along x and y, respectively. The signal attenuation ratio was representative of the proportion of the signal that remains from spatial phase gradient dephasing. A ratio of one indicated no signal loss, while lower values indicated signal loss from rapidly changing phase across an image. The mean across the masked signal attenuation map was computed to evaluate differences between levels of gradient moment nulling.

2.5 | ADC evaluation

Complex imaging data was also averaged. First, the low-frequency background phase was estimated by applying a hamming-filter (75% of the matrix size) to the k-space data.[22] Then, this background phase was subtracted from the complex dataset. The real-value component of the data was then averaged across repetitions. The ADC was then computed pixel-wise from this real-valued dataset. This was repeated for each experiment and level of moment nulling to evaluate changes in ADC for different moment nulling levels.

For a given moment nulling level, pixels were pooled from all volunteers, slices and TDs and the distributions were visualized in histogram plots (bin width = 0.05, bin range = [0,3] $\mu m^2/ms$). For visualization, ADC values exceeding 3 $\mu m^2/ms$ were assigned the last bin. Medians and 25th and 75th percentiles were reported, excluding ADC values greater than 3 $\mu m^2/ms$ from the computation. For statistical analysis, mean ADC across image, slice, and TD were computed per volunteer and for each moment nulling and then subsequently assessed for significant differences ($p < 0.05$).

2.6 | Statistical analysis

The net mean temporal phase SD (σ_ϕ) and spatial phase gradient ($\mu_{\|\phi\|}$) were calculated for across all volunteers, slices, and TD and were reported for a given diffusion direction and moment nulling level (Table S1).

Mean Temporal phase SD and spatial phase gradients across all volunteers were then evaluated for statistical significance between levels of gradient moment nulling for an individual slice, TD, and diffusion direction. Groups were first assessed for normality using the Shapiro–Wilk test. If the distribution was normal, a repeated-measures ANOVA was performed to test for significant differences between levels of gradient moment nulling. If significance was detected, then paired t-tests were used to assess significance between specific groups. For nonnormal distributions, the Kruskal–Wallis test was

used to assess significance between the groups, with the Wilcoxon signed-rank test then used to determine statistical significance between different levels of gradient moment nulling. For assessing differences between TDs, a repeated-measures ANOVA (for normal distributions) or the Friedman's test was used (for nonnormal distributions).[50] All post hoc testing used Holm–Sidak correction for multiple comparison. Statistics were computed using Python SciPy Statistics package.[51] A p-value of 0.05 was accepted as significant.

The percentage of t-tests in which statistical significance was detected between different gradient moment nulling levels for all slice positions and TDs for a given diffusion-encoding was reported (Table S2). The total number of t-tests evaluated for each experiment were as follows: Experiment-1: 48 cases (6 slices × 8 TD), Experiment-2: 6 cases (6 slices × 1 TD), Experiment-3: 3 cases (3 slices × 1 TD).

3 | RESULTS

3.1 | Experiment 1: fixed trigger delay neuro DWI

3.1.1 | Temporal phase SD

The largest temporal phase SDs were observed for diffusion encoding along G_z (Table S1A – yellow highlight). Temporal phase SD maps appeared reduced and spatially more uniform with M_1 and $M_1 + M_2$ gradient moment nulling (Figure 2A). Temporal phase SD at different TDs were consistently reduced with at least M_1 gradient moment nulling (Figure 2B).

A significant decrease in temporal SD with M_1 compared to M_0 occurred in 35% of t-tests. There was a significant decrease in temporal SD with $M_1 + M_2$ gradient moment nulling compared to M_0 in 68% of tests. Differences between compensating for only velocity (M_1) or added acceleration ($M_1 + M_2$) were very minimal, as 4% of tests between M_1 and $M_1 + M_2$ had a significant decrease with more moment nulling. Temporal phase SD reductions with at least M_1 compensation were consistent between slice positioning (Figure S2).

In the absence of diffusion encoding ($b = 0$), the scale of intra-voxel temporal (shot-to-shot) phase differences were smaller than during diffusion encoding. M_1 and $M_1 + M_2$ gradient moment nulling had higher temporal phase SD (Figure S3) which were significant in several cases (Table S2). Diffusion encoding along G_x and G_y had higher temporal phase SD compared to $b = 0$, but lower temporal phase SD compared to G_z (Figure S3). There were minimal significant differences observed between levels of moment nulling for diffusion encoding along G_x and G_y.

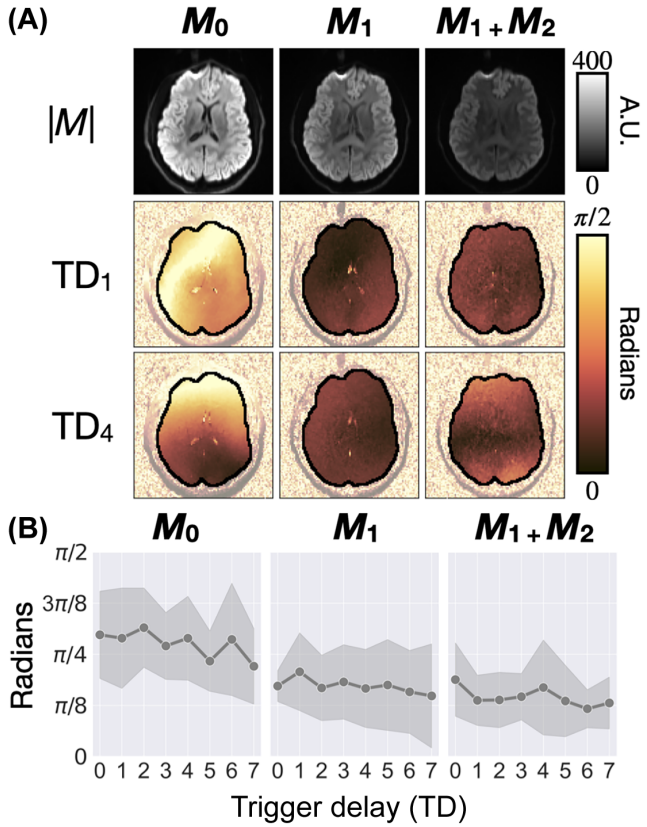

FIGURE 2 Experiment-1 temporal phase SD maps. (A) Example G_z σ_ϕ maps for TD_1 and TD_4. Temporal phase SDs were reduced with at least M_1 gradient moment nulling at different TDs. (B) Mean σ_ϕ plotted for the different TDs for the slice in (A). The confidence band represents the inter-subject SD. M_1 and $M_1 + M_2$ have consistently lower temporal phase compared to M_0. For this central slice, the reduction in σ_ϕ was significant between M_0 and M_1 in 25% of TDs and between between M_0 and $M_1 + M_2$ in 50% of TDs.

In brief, we find that M_1 and $M_1 + M_2$ moment nulling consistently reduces temporal phase SD compared to M_0 for G_z (Tables S1A and S2A). G_x and G_y diffusion encoding trended with smaller temporal phase SDs compared to G_z diffusion encoding and had similar temporal phase SDs between different moment nulling levels.

3.1.2 | Spatial phase gradient

For G_z, the average spatial phase gradient ($\mu_{\|\phi\|}$) maps for a given volunteer had a TD-dependent spatial phase gradient (Figure 3A) and slice-dependent spatial phase gradient. Slices closer to the brainstem had significantly higher spatial phase gradients at TD_0 (Figure S4). M_1 gradient moment nulling assisted in reducing the spatial phase gradient at TD_0. (Figure 3B). Gradient moment nulling

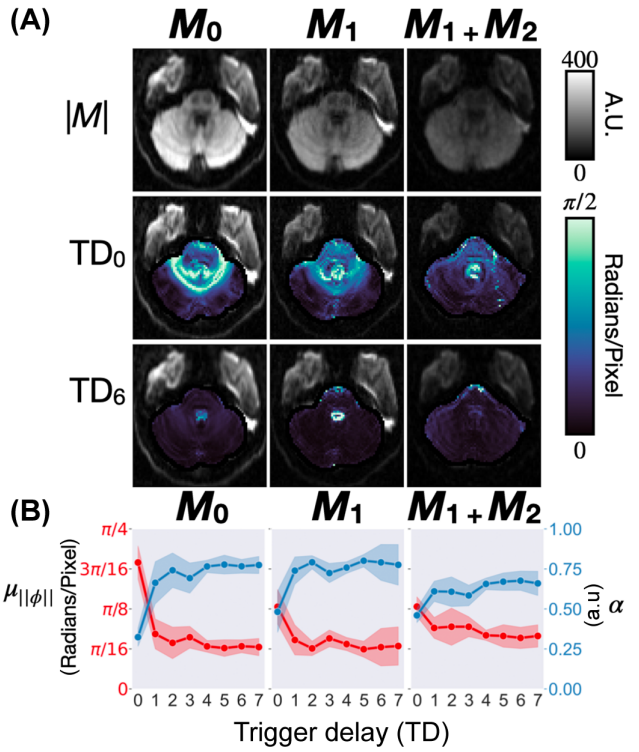

FIGURE 3 Experiment-1 spatial phase gradient maps. (A) Representative G_z $\mu_{||\phi||}$ maps of early and late TDs for a lower brain slice. There was an increase in mean spatial phase for TD_0 compared to TD_6. (B) Plot of mean spatial gradient ($\mu_{||\phi||}$) for different TEs for the slice in (A) (in red) and the paired attenuation ratio (α) (in blue). The confidence band was representative of the SD between subjects. $\mu_{||\phi||}$ was higher at earlier TDs, which was minimized with at least M_1 gradient moment nulling. α was lower at the same TD and improved with at least M_1 moment nulling. At TD_0, this reduction in $\mu_{||\phi||}$ was significant from M_0 to M_1 and from M_0 to $M_1 + M_2$ ($p < 0.05$). For latter TEs, M_0 and M_1 have higher α than $M_1 + M_2$.

significantly reduced the spatial phase gradient in 23% of cases for M_1 compared to M_0. However, $M_1 + M_2$ gradient moment nulling generally increased spatial phase gradients compared to M_0 (63% of cases).

For non-diffusion encoding ($b = 0$), average spatial phase gradients were smaller compared to G_z and similar between TDs (Figure S5). On these small scales, spatial phase gradient trends were TE-dependent, 54% of t-tests for M_1 compared to M_0 and 85% of tests for $M_1 + M_2$ compared to M_0 had significantly higher spatial phase gradients.

Diffusion encoding along G_x and G_y on average had higher spatial phase gradients compared to $b = 0$, but smaller spatial phase gradients compared to G_z (Figure S5). Spatial phase gradients trended higher at TD_0 compared to later TDs for lower brain slices. For both G_x and G_y diffusion encoding, M_1 and $M_1 + M_2$ moment nulling tended to have significantly higher spatial phase gradients compared to M_0 (Table S2).

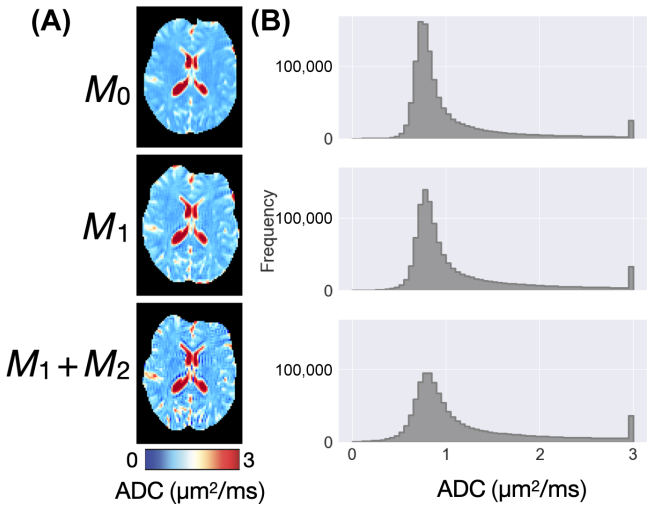

FIGURE 4 Experiment-1 apparent diffusion coefficient (ADC) evaluation. (A) Example ADC maps of a central brain slice from one volunteer demonstrated high consistency between moment nulling levels. $M_1 + M_2$ maps appeared noisier in comparison to others. (B) Distribution of ADC values for the neuroimaging data pooling pixels from all delay time (TD), repetitions, and slices for all volunteers. Distributions were very close between different moment nulling levels, with slightly elevated ADC observed in $M_1 + M_2$ moment nulling. Pixels with ADC values greater than 3 $\mu m^2/ms$ were assigned the last histogram bin.

Overall, M_1 reduced the spatial phase gradient for diffusion encoding along G_z; however, $M_1 + M_2$ more often increased the spatial phase gradient (Tables S1B and S2B). Spatial phase gradients for G_x and G_y were less than G_z, but M_1 and $M_1 + M_2$ tended to significantly increase the spatial phase gradients compared to M_0.

3.1.3 | Signal attenuation ratio

For G_z, the signal attenuation ratio (α) trended opposite of the spatial phase gradient (Figure 3B) as spatial phase reductions resulted in a higher ratio, indicating less signal losses. The first TD had a lower α, correlating to the greater spatial phase variations. At later TDs, α was similar between M_0 and M_1, but was lower for $M_1 + M_2$, indicating more signal loss due to phase variation.

3.1.4 | ADC evaluation

ADC maps for $M_1 + M_2$ were noisier than M_1 and M_0 (Figure 4A). The distribution of ADC values were similar between M_0 and M_1 (Figure 4B). However, there was a significant increase in the ADC from M_0 to $M_1 + M_2$ ($p < 0.01$). The median ADC were as follows:

0.82 [0.73,1.06] $\mu m^2/ms$, 0.87 [0.76,1.19] $\mu m^2/ms$, 0.92 [0.77,1.34] $\mu m^2/ms$ for M_0, M_1, and $M_1 + M_2$, respectively.

3.2 | Experiment-2: mixed trigger delay neuro DWI

3.2.1 | Temporal phase SD

Highest mean temporal phase SDs (σ_ϕ) were observed for G_z and were greater than Exp-1 (Table S1A – yellow highlight). The mean temporal phase SD maps from the bootstraps appear overall flatter than the individual TD temporal phase SD maps from Experiment-1 (Figure 5A). Across all volunteers, there was a larger reduction in mean temporal phase SD from M_0 to $M_1 + M_2$ versus from M_0 to M_1 (Figure 5B). This reduction in temporal phase SD from M_0 to $M_1 + M_2$ was significant (at least $p < 0.05$) in five of the six slices. For a given gradient moment nulling level, the temporal phase SD was consistent between slices (Figure S6). The confidence interval of the temporal phase SD ($d\sigma_\phi$) was very similar for the different levels of gradient moment nulling and generally not significantly different between gradient moment nulling levels.

Mean temporal phase SD (σ_ϕ) and the confidence interval of uncertainty ($d\sigma_\phi$) for G_x and G_y diffusion encoding were slightly lower than values observed for G_z (Figure S7). The difference between moment nulling levels σ_ϕ and $d\sigma_\phi$ was generally not significant.

For the $b = 0$ images, the temporal phase SD was smaller compared to diffusion encoding along G_x, G_y, and G_z (Figure S7). There were significantly higher temporal phase SDs from M_0 to M_1 and from M_1 to $M_1 + M2$.

In general, significant decreases in temporal phase SD were only observed from M_0 to $M_1 + M_2$ for G_z diffusion encoding (Table S2B). For G_x and G_y there were generally no significant differences between levels of gradient moment nulling while for $b = 0$ there were significant increases in temporal phase SD.

3.2.2 | Spatial phase gradient

Net mean spatial phase gradients were greatest for G_z compared to G_x and G_y (Table S1B – yellow highlight). Spatial phase gradients varied across slice positions, with larger spatial phase gradients near the brainstem (Figure S8). M_1 spatial phase gradient maps appear qualitatively lower than M_0 while $M_1 + M_2$ maps appear qualitatively larger than M_0 (Figure 6A) which was consistent across volunteers (Figure 6B). There was a significant decrease in the mean spatial phase gradient from M_0 to M_1 in inferior brain slices and superior cortex brain slice; however, there were no significant differences in central brain slices (Figure S8). There was a significant increase in spatial phase gradient from M_0 to $M_1 + M_2$ in four of six slices and a significant increase from M_1 to $M_1 + M_2$ in five of six slices. The confidence interval of the spatial phase gradient across bootstraps had a larger spread than the mean across volunteers. There was a significant ($p < 0.01$) decrease in the 95% CI from M_0 to M_1 in three of six slices and a significant ($p < 0.05$) decrease in the spatial phase gradient 95% CI in two of six slices.

For G_x and G_y the spatial phase gradient for $M_1 + M_2$ trended higher than M_0 and M_1 gradient moment nulling (Figure S9). M_1 and $M_1 + M_2$ were often significantly higher than M_0 (Table S2).

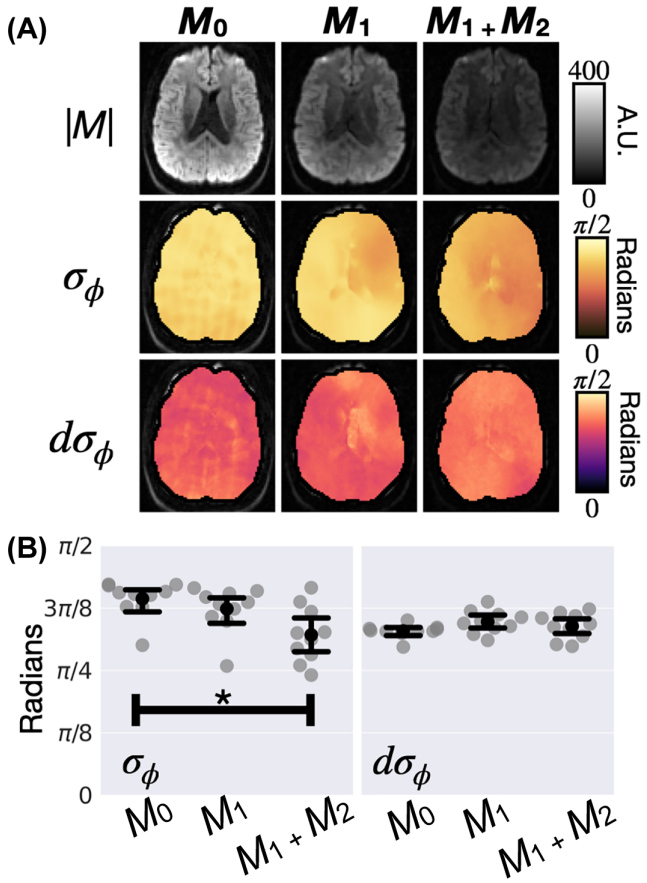

FIGURE 5 Experiment-2 mean temporal phase SD (σ_ϕ) maps for G_z. (A) Example mean σ_ϕ and $d\sigma_\phi$ for a central brain slice after 1000 bootstraps. Temporal phase SD maps were spatially uniform and maps qualitatively appeared lower with M_1 and $M_1 + M_2$ gradient moment nulling. (B) Mean σ_ϕ and $d\sigma_\phi$ plotted for the same slice in (A). The black dot represents the mean and the lines represent the SD, with the gray dots individual volunteer means. For this central slice, $M_1 + M_2$ had significantly ($p < 0.01$) lower temporal phase SD compared to M_0. The confidence interval of σ_ϕ ($d\sigma_\phi$) was similar between levels of gradient moment nulling. Average σ_ϕ was higher than in Experiment-1 (Table S1).

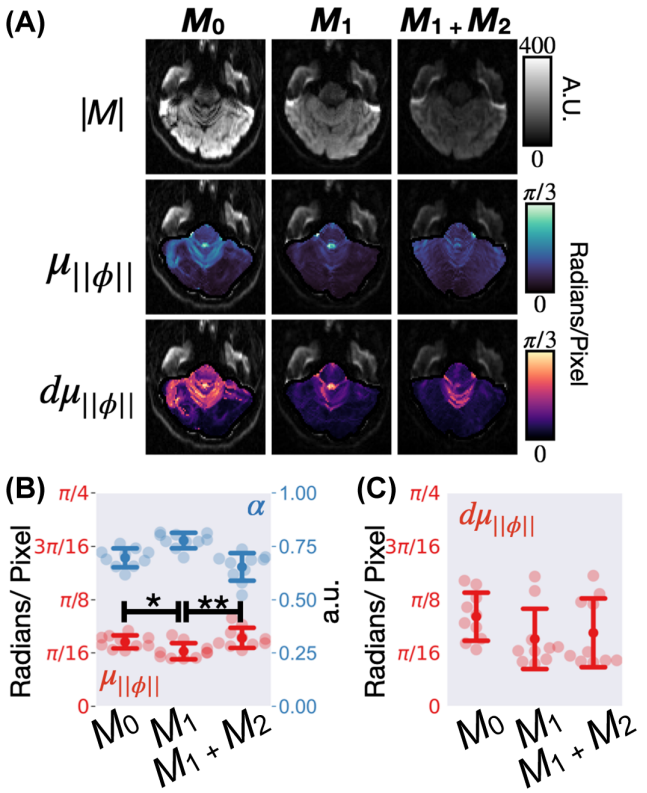

FIGURE 6 Experiment-2 mean spatial phase gradient maps. (A) Example mean G_z $\mu_{||\phi||}$ and $d\mu_{||\phi||}$ for a lower brain slice after 1000 bootstraps. Spatial phase gradient maps towards the brainstem had large spatial phase gradients. Spatial phase gradients trended lower with M_1 gradient moment nulling, but were higher with $M_1 + M_2$. (B) Mean $\mu_{||\phi||}$ plotted for the same slice in (A) (in red) and the corresponding attenuation ratio (α) (in blue). Solid red or blue dot represents mean and the lines the SD between volunteers, with the light dots individual volunteer means. For this slice, there was a significant decrease in spatial phase gradient ($p < 0.05$) from M_0 to M_1 but a significant ($p < 0.01$) increase from M_1 to $M_1 + M_2$. (C) $d\mu_{||\phi||}$ plotted for same slice as (A) showed no significant differences between amounts of moment nulling.

The scale of spatial phase gradients were much smaller for $b = 0$ images. Trends in the $b = 0$ images correspond to TE changes, as M_1 and $M_1 + M_2$ moment nulling resulted in higher spatial phase gradients.

Broadly, spatial phase gradients were on a much smaller scale than temporal phase SDs (Table S1). For G_z there were no significant differences between M_0 and M_1, although spatial phase gradients trended lower with M_1 (Tables S1B and S2B). Significant increases were otherwise observed from M_0 to $M_1 + M_2$. Significant increases were also observed with G_x, G_y, and $b = 0$ diffusion encoding.

3.2.3 | Signal attenuation ratio

For G_z, the signal attenuation ratio (α) trended opposite of the spatial phase gradient (Figure 6B). M_1 had a higher α than M_0, corresponding to a significant decrease in spatial phase gradient compared to M_0. $M_1 + M_2$ had a lower α than M_1 and trended similar to M_0.

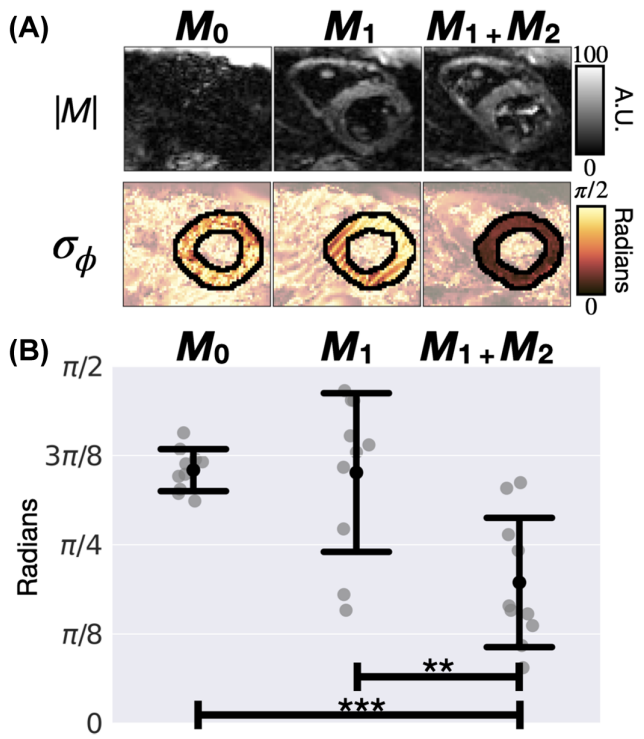

FIGURE 7 Experiment-3 temporal phase SD maps. (A) Example G_z σ_ϕ maps for a mid-ventricular slice. Qualitatively, temporal phase SD was noise-like for M_0, structured with M_1 but not necessarily reduced, and much more consistent and smaller with $M_1 + M_2$ moment nulling. (B) Mean σ_ϕ plotted for all the volunteers for the slice in (A). Group mean was represented by the black dot and the SD between volunteers indicated by the black line. $M_1 + M_2$ had consistently significantly lower temporal phase compared to M_0 and M_1. Significance indicated by the stars (** $p < 0.01$, *** $p < 0.001$).

3.3 | Experiment-3: fixed trigger delay cardiac DWI

3.3.1 | Temporal phase SD

Temporal phase SDs were higher for G_x, G_y, and G_z diffusion encoding in comparison to $b = 0$ (Table S1A – yellow highlight). Temporal phase SD maps for G_z appear noise-like for M_0. The maps were reduced, but structured with M_1, and significantly reduced and more uniform with $M_1 + M_2$ (Figure 7A). This corresponds to the lack of evident magnitude signal for M_0 that was then resolved with M_1 and generally improved with $M_1 + M_2$. Temporal phase SD was consistently significantly reduced (at least $p < 0.01$) with $M_1 + M_2$ gradient moment nulling (Figure 7B). $M_1 + M_2$ moment nulling significantly (at least $p < 0.05$)

reduced temporal phase SD compared to M_0 and M_1 across all slices (Figure S10).

Like G_z diffusion encoding, G_x and G_y diffusion encoding exhibited significant reductions (at least $p < 0.05$) in temporal phase SD with $M_1 + M_2$ gradient moment nulling (Figure S10). This was consistent across all slices. M_1 temporal phase SDs were not significantly different than M_0. Without diffusion encoding ($b = 0$), temporal phase SDs were lower than G_x, G_y, and G_z diffusion encoding. No significant differences were detected between different levels of gradient moment nulling for $b = 0$.

Overall, higher temporal phase SDs were observed across diffusion directions for Cardiac DWI compared to Brain DWI (Table S1A – yellow highlight). Temporal phase SD maps were smoother and greatly reduced with increasing gradient moment nulling. $M_1 + M_2$ significantly reduced temporal phase SDs across all slices for G_x, G_y, and G_z diffusion encoding (Table S2A).

3.3.2 | Spatial phase gradient

For diffusion encoding along G_z, the average spatial gradient ($\mu_{||\phi||}$) without gradient moment nulling was very noise like and elevated (Figure 8A). This spatial phase gradient was reduced with M_1 gradient moment nulling, with some variation apparent across a map. $M_1 + M_2$ reduces the spatial phase gradient further, appearing flatter across a map. For mid-ventricular slices, the average spatial phase gradient $\mu_{||\phi||}$ was significantly reduced when increasing the level of gradient moment nulling from M_0 to M_1 or $M_1 + M_2$ and from M_1 to $M_1 + M_2$ (Figure 8B). M_1 moment nulling had significantly lower spatial phase gradient compared to M_0 ($p < 0.001$) and $M_1 + M_2$ had significantly lower spatial phase gradient compared to M_0 ($p < 0.001$) and M_1 ($p < 0.01$). These trends were consistent across slices (Figure S11).

The average spatial phase gradients of G_x and G_y diffusion encoding had similar significant (at least $p < 0.05$) reductions with increasing levels of gradient moment nulling from M_0 to M_1 and M_0 to $M_1 + M_2$ (Figure S11 and Table S2B). M_1 was significantly lower than M_0 (at least $p < 0.05$). $M_1 + M_2$ was always significantly lower than M_0 (at least $p < 0.01$) and almost always significantly lower than M_1 (at least $p < 0.05$) across all slices for both G_x and G_y (Table S2).

In the absence of diffusion, the overall average spatial phase gradient was lower than diffusion encoding along G_x, G_y, or G_z; however, the average spatial phase gradient increased significantly ($p < 0.05$) from M_0 to M_1 and from M_0 to $M_1 + M_2$ (Figure S10).

In brief, spatial phase gradients were larger in Cardiac DWI compared to Neuro DWI (Table S1B).

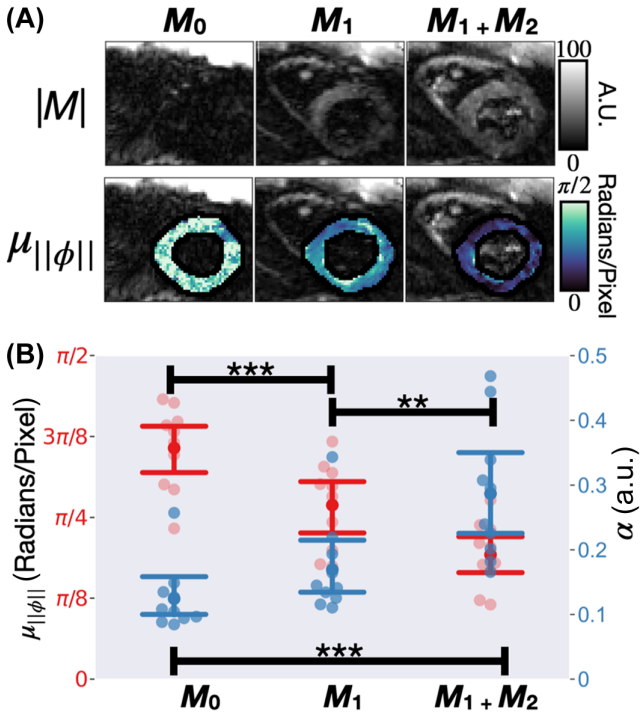

FIGURE 8 Experiment-3 spatial phase gradient maps. (A) Example G_z $\mu_{||\phi||}$ maps for a mid-ventricular slice. Maps were less-noise like and $\mu_{||\phi||}$ reduced with increasing gradient moment nulling. (B) Mean $\mu_{||\phi||}$ plotted for all the volunteers for the slice in (A) (in red) with the paired attenuation ratio (α) (in blue). Group mean is represented by the solid dot and the SD between volunteers indicated by the solid line. Average $\mu_{||\phi||}$ was significantly reduced with M_1 ($p < 0.001$) and $M_1 + M_2$ ($p < 0.001$) gradient moment nulling. $M_1 + M_2$ also had significantly ($p < 0.01$) lower average spatial phase gradient than M_1. This spatial phase gradient reduction resulted in a higher attenuation ratio, indicating less signal loss due to the phase with $M_1 + M_2$ moment nulling. Significance is indicated by the stars (** $p < 0.01$, *** $p < 0.001$).

$M_1 + M_2$ gradient moment nulling significantly reduced spatial phase gradients across slices, volunteers, and diffusion encoding orientations, compared to M_0 (Table S2B – yellow highlight). $M_1 + M_2$ was also often significantly lower than M_1, generating smoother spatial phase gradient maps compared to less gradient moment nulling. For $b = 0$ images, the scale of spatial phase gradients was much smaller but spatial phase gradient increased with M_1 and $M_1 + M_2$ gradient moment nulling.

3.3.3 | Signal attenuation ratio

The signal attenuation ratio trended opposite of the spatial phase gradient (Figure 8B). The scale of the signal attenuation ratio for the cardiac data was lower than the neuroimaging datasets. $M_1 + M_2$ had the highest signal attenuation ratio, indicative of more motion robustness.

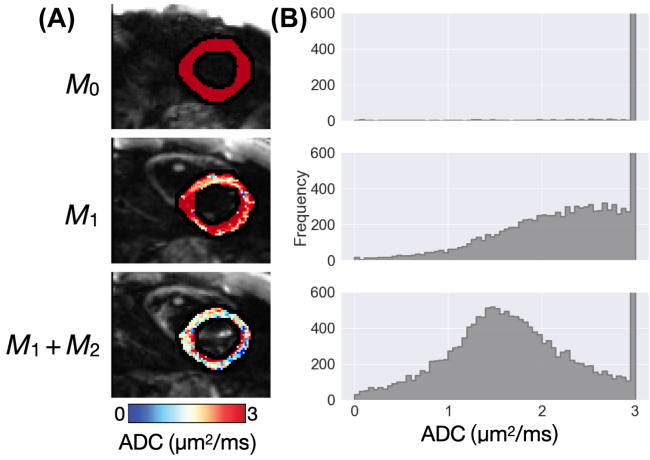

FIGURE 9 Experiment-3 apparent diffusion coefficient (ADC) evaluation. (A) Example ADC maps of the myocardium of a mid-ventricular slice demonstrated elevated and highly inaccurate ADC for M_0 moment nulling, and reduced ADC with M_1 and particularly $M_1 + M_2$. (B) Distribution of ADC pooled from pixels from all volunteers and slices. Pixels with ADC values greater than 3 $\mu m^2/ms$ were assigned the last histogram bin. ADC of the myocardium was reduced with $M_1 + M_2$ moment nulling.

3.3.4 | ADC evaluation

ADC maps appear elevated and highly inaccurate for M_0 and were significantly ($p < 0.01$) lower for both M_1 and $M_1 + M_2$ (Figure 9A). $M_1 + M_2$ tended to have lower ADCs than M_1. Moment nulling reduced the ADC values of the myocardium. $M_1 + M_2$ had a less skewed distribution of ADC compared to M_1 and M_0 (Figure 9B). The median ADC for M_0 was 2.00 [1.27, 2.57] $\mu m^2/ms$, M_1 was 2.20 [1.72,2.60] $\mu m^2/ms$ and $M_1 + M_2$ was 1.60 [1.22,2.04] $\mu m^2/ms$.

4 | DISCUSSION

This study investigated the amount of phase consistency in DWI enabled through the use of gradient moment nulling by evaluating the temporal phase SD and spatial phase gradient for three different experiments. In Experiment-1, we demonstrated how M_1 gradient moment nulling reduced temporal phase SDs and spatial phase gradients compared to M_0 for G_z. In Experiment-2, we observed that $M_1 + M_2$ significantly reduced temporal phase SD for G_y and G_z, but only M_1 significantly reduced spatial phase gradients for G_x and G_z. Otherwise, increased moment nulling tended to significantly increase the spatial phase gradient. In Experiment-2, temporal phase SDs were higher than Experiment-1 while the spatial phase gradients were similar scale. For Experiment-3, $M_1 + M_2$ gradient moment nulling had significant reductions in temporal phase SD and spatial phase gradients, minimizing the variations between repetitions.

In both neuroimaging experiments, we observed that the effect of motion-encoding on phase consistency was most predominant when encoding along the G_z direction. This could be attributed to the pulsatile motion in the brain predominately occurring along the z-axis, originating towards the brain stem and propagating outwards from the Circle of Willis.[52-54] Because this motion was predominately superior-inferior, it was likely there was more bulk motion and resultant *intra-voxel* dephasing along that direction. Thus, since this motion can be approximated as acceleration-free, when applying M_1 motion compensation, the encoding of all velocities were rephased, such that the spatial phase gradients would be reduced and temporal phase SDs were smaller between repeated acquisitions. This motion occurred less along G_x and G_y, therefore the effectiveness of gradient moment nulling was not as large. Additionally, this motion is time-dependent, as in Experiment-1, the higher spatial phase gradients were observed at TD_0 for slices closer to the brainstem. This likely corresponds to elevated intracranial pressures and tissue motion after the transit time of the systolic impulse of the cardiac cycle[55] (Figure 3B). For $b = 0$ images (i.e., no diffusion-encoding) we observed very small temporal phase SDs and spatial phase gradients. The trends for $b = 0$ images corresponded closely to TE differences, as the longer TEs of M_1 and $M_1 + M_2$ corresponded to significantly higher temporal phase SDs and spatial phase gradients. Longer TEs accord with decreased spin-echo amplitudes, which can result in a signal attenuation of up to 40% for M_1 and around 55%–65% for $M_1 + M_2$ compared to M_0.

$M_1 + M_2$ consistently had lower temporal phase SDs compared to M_1 in the brain, but did not necessarily yield lower spatial phase gradients. This is probably because the longer diffusion footprint of $M_1 + M_2$ gradient moment nulling lengthens the TE and dominates the effect of mitigating motion sensitivity. Due to the longer TEs, the signal attenuation is inherently greater and thus there are still penalties in phase consistency despite gradient moment nulling. However, the availability of ultra-high performance gradient systems could mitigate the TE penalty.[56] The prolonged TE also likely contributed to a noisier ADC distribution and an elevated median ADC for $M_1 + M_2$. This may suggest that $M_1 + M_2$ was more sensitive to long T2 tissues (i.e., CSF) that also have higher ADCs. In addition, the shorter effective diffusion time (Δ) of motion compensated DWI would result in less sensitivity to restricted or hindered diffusion because there would not be enough time for spins to encounter diffusive barriers, resulting in elevated ADCs.[57,58]

Meanwhile, the effect of gradient moment nulling in reducing temporal phase SDs and spatial phase

gradients was very significant in the heart, along G_x, G_y, and G_z. This was likely due to the more complex three-dimensional heart motion compared to the predominately one-directional movement observed in the brain. The bulk contraction in the heart was a complex contracting and twisting motion,[59,60] thus compensating for velocity and acceleration in all three-directions proved consequential for phase consistency. $M_1 + M_2$ gradient moment nulling was most effective in the heart as it best captured and mitigated sensitivity to velocities and accelerations. Like observations in the brain, the $b = 0$ images had minimal phase variations as the acquisition was not sensitive to *intra-voxel* and *inter-voxel* phase dispersion.

Complex-averaging with background phase correction removes substantial motion-induced low spatial frequency background phase errors for all forms of gradient moment nulling. However, there can be residual phase errors, especially from motion-induced high spatial frequency phase, that if uncompensated results in ADC errors after complex averaging. We see these errors predominately in M_0 and M_1 moment-nulled cardiac DWI.

The phase stability of $M_1 + M_2$ demonstrated in this study corroborates the previous literature.[49,61] The lower spatial phase gradients we observed with $M_1 + M_2$ moment nulling at mid-systole corresponded with work by Stoeck et al. that related the phase in cardiac DWI to motion-related signal loss at different trigger-delay times.[49] Our work shows that a mid-systolic time point had a less rapidly changing phase with $M_1 + M_2$. However, we assess solely in-plane spatial phase gradients. We suspect that in the heart, through-plane spatial phase gradients would be on the same scale as the in-plane spatial phase gradients based on Stoeck et al.[49] The decreasing temporal phase SD and spatial phase gradients of M_1-nulled cardiac DWI also corresponded to previously reported flow-compensated DWI in the heart.[61] The noise-like temporal phase SDs and spatial phase gradients observed with M_0 moment nulling in cardiac DWI arises from near complete signal loss from uncompensated motion.[19] Of course, estimates of the phase as the signal decreases became increasingly noise-like. The reduced signal attenuation with $M_1 + M_2$ also resulted in ADC values that closely corresponded to the previously reported literature.[62]

Overall, the observations in this experiment may be hardware and software dependent. The commodity hardware utilized in this study was not an ultra high-performance gradient system. Therefore, the TEs in this study were quite long which introduces more *intra-voxel* and *inter-voxel* phase resulting in lower signal. This was most predominately observed in Experiment-1 and Experiment-2, as we see the spatial phase was on average higher for $M_1 + M_2$ compensation than M_0 and M_1. To note, $M_1 + M_2$ neuroimaging acquisition had a TE of 143 ms, which would be reduced by over 30% in high-performance gradient systems. This would affect the spatial phase variation of $M_1 + M_2$, which we hypothesize would be reduced with shorter TE. ECG gating or M_1 gradient moment nulling can be used to increase phase consistency and were generally available on most vendor DWI protocols.

Another limitation in our study was that we only evaluated one *b*-value per each experiment. For our cardiac DWI study, the *b*-value investigated was on the lower end of the *b*-values that are commonly used in cardiac DWI studies in order to shorten the TE when using our commodity gradient hardware. On our system, higher *b*-values would result in increased temporal phase SD and spatial phase gradients, which would subsequently contribute to additional signal attenuation. Recommendations have been made in neuroimaging,[63] abdominal imaging,[64] and cardiac imaging[65] around the optimal b-value encoding. The phase consistency would be reduced at high *b*-values due to elongated TEs and increased diffusion footprint. This impacts the effectiveness of M_1 and $M_1 + M_2$ compensation, which assume constant velocity and acceleration throughout this encoding period. Future experiments could investigate the effect of *b*-value on changing temporal variations and spatial gradients. Some signal attenuation may be mitigated with a combination of ECG-gating and motion compensation. However, this too would be application dependent and scanner-specific.

Furthermore, we acknowledge that Partial Fourier acquisitions may lead to imprecise estimates of the phase compared to Full Fourier sampling.[48] However, Partial Fourier sampling allowed us to shorten the TE on our commodity system which would otherwise be additionally prolonged.

In the brain, ECG-gating with motion compensation can also be utilized for diffusion-preparation pulses.[66,67] The use of M_1 compensation and ECG gating in diffusion prepared pulses can preserve signal from motion corruption, while not loosing the SNR from adding an amplitude stabilizer. The minimization of phase variation using ECG-gating and M_1 motion compensation has been demonstrated to be effective in a diffusion-prepared MR Fingerprinting sequence.[68] On the other hand, multishot image reconstructions can be better conditioned with both ECG-gating and M_1 motion compensation as the temporal and spatial phase between shots will be more consistent, enabling easier implementation in higher motion environments. In the heart, the phase consistency provided by $M_1 + M_2$ motion compensation was demonstrated to be on a similar scale to what was observed in neuroimaging with M_0 and M_1 motion compensation. Thus, in the future there is potential to move toward higher resolutions in the heart via multishot approaches using $M_1 + M_2$

motion compensation to minimize spatial and temporal phase variations.

5 | CONCLUSION

In this study, we assessed the effectiveness of gradient moment nulling in DWI for mitigating temporal phase variations and spatial phase gradients. We observed that in neuroimaging, the effect of ECG-gating and M_1 gradient moment nulling resulted in minimized temporal phase variations and spatial phase gradients for diffusion encoding along G_z. However, for diffusion encoding along G_x and G_y, there were incidences where moment nulling resulted in phase instability, particularly with $M_1 + M_2$ moment nulling, owing to longer TE times and decreased SNR. In the heart, $M_1 + M_2$ gradient moment nulling significantly reduced temporal phase SD and spatial phase gradients along G_x, G_y, and G_z. The combination of reducing these two phase metrics resulted in a more consistent and smoother phase, that would better enable imaging techniques such as multishot or diffusion-preparation pulses. Overall, this was the first characterization of phase consistency enabled by gradient moment nulling on a commodity MRI system for both brain and cardiac DWI.

ACKNOWLEDGMENTS

We thank Jarrett Rosenberg for meaningful discussion on statistical analysis and we thank Julio A. Oscanoa for assistance in formatting the manuscript using the Latex Template.

DATA AVAILABILITY STATEMENT

In the spirit of reproducible research, the code and data necessary to reproduce the results in the paper will be available at https://github.com/ahannum/dwi_phase.

ORCID

Ariel J. Hannum https://orcid.org/0000-0003-0650-574X
Tyler E. Cork https://orcid.org/0000-0001-5759-5322
Kawin Setsompop https://orcid.org/0000-0003-0455-7634
Daniel B. Ennis https://orcid.org/0000-0001-7435-1311

REFERENCES

1. Le Bihan D, Breton E. Imagerie de diffusion in-vivo par résonance magnétique nucléaire. *C R Acad Sci*. 1985;93:27-34.
2. Taylor DG, Bushell MC. The spatial mapping of translational diffusion coefficients by the NMR imaging technique. *Phys Med Biol*. 1985;30:345-349.
3. Soares J, Marques P, Alves V, Sousa N. A Hitchhiker's guide to diffusion tensor imaging. *Front Neurosci*. 2013;7:31.
4. Le Bihan D, Breton E, Lallemand D, Grenier P, Cabanis E, Laval-Jeantet M. MR imaging of intra-voxel incoherent motions: application to diffusion and perfusion in neurologic disorders. *Radiology*. 1986;161:401-407.
5. Le Bihan D. Diffusion MRI: what water tells us about the brain. *EMBO Mol Med*. 2014;6:569-573.
6. Ablefoni M, Surup H, Ehrengut C, et al. Diagnostic benefit of high b-value computed diffusion-weighted imaging in patients with hepatic metastasis. *J Clin Med*. 2021;10:5289.
7. Saito K, Tajima Y, Harada TL. Diffusion-weighted imaging of the liver: current applications. *World J Radiol*. 2016;8:857-867.
8. Partridge SC, McDonald ES. Diffusion weighted MRI of the breast: protocol optimization, guidelines for interpretation, and potential clinical applications. *Magn Reson Imaging Clin N Am*. 2013;21:601-624.
9. Amornsiripanitch N, Bickelhaupt S, Shin HJ, et al. Diffusion-weighted MRI for unenhanced breast cancer screening. *Radiology*. 2019;293:504-520.
10. Khalique Z, Ferreira PF, Scott AD, Nielles-Vallespin S, Firmin DN, Pennell DJ. Diffusion tensor cardiovascular magnetic resonance imaging: a clinical perspective. *JACC Cardiovasc Imaging*. 2020;13:1235-1255.
11. Anderson AW, Gore JC. Analysis and correction of motion artifacts in diffusion weighted imaging. *Magn Reson Med*. 1994;32:379-387.
12. Trouard TP, Sabharwal Y, Altbach MI, Gmitro AF. Analysis and comparison of motion-correction techniques in diffusion-weighted imaging. *J Magn Reson Imaging*. 1996;6:925-935.
13. Chenevert TL, Pipe JG. Effect of bulk tissue motion on quantitative perfusion and diffusion magnetic resonance imaging. *Magn Reson Med*. 1991;19:261-265.
14. O'Halloran RL, Holdsworth S, Aksoy M, Bammer R. Model for the correction of motion-induced phase errors in multishot diffusion-weighted-MRI of the head: are cardiac-motion-induced phase errors reproducible from beat-to-beat? *Magn Reson Med*. 2012;68:430-440.
15. Robson MD, Anderson AW, Gore JC. Diffusion-weighted multiple shot echo planar imaging of humans without navigation. *Magn Reson Med*. 1997;38:82-88.
16. Atkinson D, Porter DA, Hill DLG, Calamante F, Connelly A. Sampling and reconstruction effects due to motion in diffusion-weighted interleaved echo planar imaging. *Magn Reson Med*. 2000;44:101-109.
17. Reese TG, Wedeen VJ, Weisskoff RM. Measuring diffusion in the presence of material strain. *J Magn Reson*. 1996;112:253-258.
18. Mekkaoui I, Moulin K, Croisille P, Pousin J, Viallon M. Quantifying the effect of tissue deformation on diffusion-weighted MRI: a mathematical model and an efficient simulation framework applied to cardiac diffusion imaging. *Phys Med Biol*. 2016;61:5662-5686.
19. Wedeen VJ, Weisskoff RM, Poncelet BP. MRI signal void due to in-plane motion is all-or-none. *Magn Reson Med*. 1994;32:116-120.
20. Miller KL, Pauly JM. Nonlinear phase correction for navigated diffusion imaging. *Magn Reson Med*. 2003;50:343-353.
21. Sloots JJ, Froeling M, Biessels GJ, Zwanenburg JMM. Dynamic brain ADC variations over the cardiac cycle and their relation to tissue strain assessed with DENSE at high-field MRI. *Magn Reson Med*. 2022;88:266-279.

22. Eichner C, Cauley SF, Cohen-Adad J, et al. Real diffusion-weighted MRI enabling true signal averaging and increased diffusion contrast. *Neuroimage*. 2015;122:373-384.
23. Raspe J, McTavish S, Weiss K, Peeters JM, Karampinos DC, Van AT. On intra-voxel dephasing in liver diffusion-weighted imaging. In *Proceedings of the 2023 ISMRM & ISMRT Annual Meeting & Exhibition*. Toronto, CA; 2023:2443.
24. Edelman RR, Gaa J, Wedeen VJ, et al. In vivo measurement of water diffusion in the human heart. *Magn Reson Med*. 1994;32:423-428.
25. Koh DM, Collins DJ. Diffusion-weighted MRI in the body: applications and challenges in oncology. *Ajr Am J Roentgenol*. 2007;188:1622-1635.
26. Kwee TC, Takahara T, Niwa T, et al. Influence of cardiac motion on diffusion-weighted magnetic resonance imaging of the liver. *Magma*. 2009;22:319-325.
27. Butts K, Riederer SJ, Ehman RL, Thompson RM, Jack CR. Interleaved echo planar imaging on a standard MRI system. *Magn Reson Med*. 1994;31:67-72.
28. Chen NK, Guidon A, Chang HC, Song AW. A robust multi-shot scan strategy for high-resolution diffusion weighted MRI enabled by multiplexed sensitivity-encoding (MUSE). *Neuroimage*. 2013;72:41-47.
29. Hu Y, Levine EG, Tian Q, et al. Motion-robust reconstruction of multishot diffusion-weighted images without phase estimation through locally low-rank regularization. *Magn Reson Med*. 2019;81:1181-1190.
30. Holdsworth SJ, Skare S, Newbould RD, Guzmann R, Blevins NH, Bammer R. Readout-segmented EPI for rapid high resolution diffusion imaging at 3T. *Eur J Radiol*. 2008;65:36-46.
31. Porter DA, Heidemann RM. High resolution diffusion-weighted imaging using readout-segmented echo-planar imaging, parallel imaging and a two-dimensional navigator-based reacquisition. *Magn Reson Med*. 2009;62:468-475.
32. Enzmann D, Pelc N. Brain motion: measurement with phase-contrast MR imaging. *Radiology*. 1992;185:653-660.
33. Greitz D, Wirestam R, Franck A, Nordell B, Thomsen C, Stahlberg F. Pulsatile brain movement and associated hydrodynamics studied by magnetic resonance phase imaging. *Neuroradiology*. 1992;34:370-380.
34. Poncelet B, Wedeen V, Weisskoff R, Cohen M. Brain parenchyma motion: measurement with cine echo-planar MR imaging. *Radiology*. 1992;185:645-651.
35. Lewis S, Dyvorne H, Cui Y, Taouli B. Diffusion-weighted imaging of the liver: techniques and applications. *Magn Reson Imaging Clin N Am*. 2014;22:373-395.
36. Haacke EM, Lenz GW. Improving MR image quality in the presence of motion by using rephasing gradients. *Am J Roentgenol*. 1987;148:1251-1258.
37. Ozaki M, Inoue Y, Miyati T, et al. Motion artifact reduction of diffusion-weighted MRI of the liver: use of velocity-compensated diffusion gradients combined with tetrahedral gradients. *J Magn Reson Imaging*. 2013;37:172-178.
38. McTavish S, van AT, Peeters JM, et al. Motion compensated renal diffusion weighted imaging. *Magn Reson Med*. 2023;89:144-160.
39. Stoeck CT, Von Deuster C, GeneT M, Atkinson D, Kozerke S. Second-order motion-compensated spin echo diffusion tensor imaging of the human heart. *Magn Reson Med*. 2016;75:1669-1676.
40. Moulin K, Croisille P, Feiweier T, et al. In vivo free-breathing DTI and IVIM of the whole human heart using a real-time slice-followed SE-EPI navigator-based sequence: a reproducibility study in healthy volunteers. *Magn Reson Med*. 2016;76:70-82.
41. Aliotta E, Moulin K, Magrath P, Ennis DB. Quantifying precision in cardiac diffusion tensor imaging with second-order motion-compensated convex optimized diffusion encoding. *Magn Reson Med*. 2018;80:1074-1087.
42. Rapacchi S, Wen H, Viallon M, et al. Low b-value diffusion-weighted cardiac magnetic resonance imaging: initial results in humans using an optimal time-window imaging approach. *Invest Radiol*. 2011;46:751-758.
43. Moulin K, Verzhbinsky IA, Maforo NG, Perotti LE, Ennis DB. Probing cardiomyocyte mobility with multi-phase cardiac diffusion tensor MRI. *PLoS One*. 2020;15:e0241996.
44. Cork TE, Moulin K, Middione MJ, Ennis DB. The effects of motion compensated encoding waveforms in cardiac diffusion tensor imaging: a moving phantom study. *In Proceedings of the SCMR 24th Annual Meeting*. (Virtual Meeting). 2021:943259.
45. Garyfallidis E, Brett M, Amirbekian B, et al. Dipy, a library for the analysis of diffusion MRI data. *Front Neuroinform*. 2014;8:8.
46. Smith SM. Fast robust automated brain extraction. *Hum Brain Mapp*. 2002;17:143-155.
47. Nolden M, Zelzer S, Seitel A, et al. The medical imaging interaction toolkit: challenges and advances: 10 years of open-source development. *Int J Comput Assist Radiol Surg*. 2013;8:607-620.
48. Bernstein MA, King KF, Zhou XJ. *Handbook of MRI Pulse Sequences*. Elsevier Academic Press; 2004.
49. Stoeck CT, von Deuster C, van Gorkum RJH, Kozerke S. Motion and eddy current-induced signal dephasing in in vivo cardiac DTI. *Magn Reson Med*. 2020;84:277-288.
50. Holm S. A simple sequentially Rejective multiple test procedure. *Scand J Stat*. 1979;6:65-70.
51. Virtanen P, Gommers R, Oliphant TE, et al. SciPy 1.0: fundamental algorithms for scientific computing in python. *Nat Methods*. 2020;17:261-272.
52. Weaver JB, Pattison AJ, McGarry MD, et al. Brain mechanical property measurement using MRE with intrinsic activation. *Phys Med Biol*. 2012;57:7275-7287.
53. Pahlavian SH, Oshinski J, Zhong X, Loth F, Amini R. Regional quantification of brain tissue strain using displacement-encoding with stimulated echoes magnetic resonance imaging. *J Biomech Eng*. 2018;140:081010.
54. Terem I, Dang L, Champagne A, et al. 3D amplified MRI (aMRI). *Magn Reson Med*. 2021;86:1674-1686.
55. Wagshul ME, Eide PK, Madsen JR. The pulsating brain: a review of experimental and clinical studies of intracranial pulsatility. *Fluids Barriers CNS*. 2011;8:5.
56. Michael ES, Hennel F, Pruessmann KP. Motion-compensated diffusion encoding in multi-shot human brain acquisitions: insights using high-performance gradients. *Magn Reson Med*. 2024;92:556-572.
57. Spinner GR, Stoeck CT, Mathez L, von Deuster C, Federau C, Kozerke S. On probing intravoxel incoherent motion in the heart-spin-echo versus stimulated-echo DWI. *Magn Reson Med*. 2019;82:1150-1163.
58. Alemany I, Rose JN, Ferreira PF, et al. Realistic numerical simulations of diffusion tensor cardiovascular magnetic resonance: the effects of perfusion and membrane permeability. *Magn Reson Med*. 2023;90:1641-1656.

59. Wang VY, Nielsen PMF, Nash MP. Image-based predictive Modeling of heart mechanics. *Annu Rev Biomed Eng*. 2015;17:351-383.
60. Peirlinck M, Costabal FS, Yao J, et al. Precision medicine in human heart modeling: perspectives, challenges, and opportunities. *Biomech Model Mechanobiol*. 2021;20:803-831.
61. Gamper U, Boesiger P, Kozerke S. Diffusion imaging of the in vivo heart using spin echoes–considerations on bulk motion sensitivity. *Magn Reson Med*. 2007;57:331-337.
62. Moulin K, Stoeck CT, Axel L, et al. In vivo cardiac diffusion imaging without motion-compensation leads to unreasonably high diffusivity. *J Magn Reson Imaging*. 2023;58:1990-1991.
63. Jones DK, Horsfield MA, Simmons A. Optimal strategies for measuring diffusion in anisotropic systems by magnetic resonance imaging. *Magn Reson Med*. 1999;42:515-525.
64. Tachibana Y, Aida N, Niwa T, et al. Analysis of multiple B-value diffusion-weighted imaging in pediatric acute encephalopathy. *PLoS One*. 2013;8:e63869.
65. Scott AD, Ferreira PF, Nielles-Vallespin S, et al. Optimal diffusion weighting for in vivo cardiac diffusion tensor imaging. *Magn Reson Med*. 2015;74:420-430.
66. Lu L, Erokwu B, Lee G, et al. Diffusion-prepared fast imaging with steady-state free precession (DP-FISP): a rapid diffusion MRI technique at 7 T. *Magn Reson Med*. 2012;68:868-873.
67. Gao Y, Han F, Zhou Z, et al. Multishot diffusion-prepared magnitude-stabilized balanced steady-state free precession sequence for distortion-free diffusion imaging. *Magn Reson Med*. 2019;81:2374-2384.
68. Cao X, Liao C, Zhou Z, et al. DTI-MR fingerprinting for rapid high-resolution whole-brain T1,T2, proton density, ADC, and fractional anisotropy mapping. *Magn Reson Med*. 2024;91:987-1001.

SUPPORTING INFORMATION

Additional supporting information may be found in the online version of the article at the publisher's website.

Table S1. Net mean temporal phase SD and spatial phase gradients.

Table S2. Percentage of significant ($p < 0.05$) t-tests.

Figure S1. Gradient waveforms and their moments for each neuro and cardiac experiment. (A) Neuro – M_0 waveform, (B) Neuro – M_1 waveform, (C) Neuro – $M_1 + M_2$ waveform, (D) Cardiac – M_0 waveform, (E) Cardiac - M_1 waveform, (F) Cardiac - $M_1 + M_2$ waveform. Moments were scaled by maximum value to be unitless in the subfigures. Imaging parameters for these protocols were found in Table 1.

Figure S2. Experiment-1 temporal phase SD. Net mean temporal phase SD (σ_ϕ) of different slices for G_z diffusion-encoding. Each row corresponds to the slice visualized in the bSSFP image to the left. The solid line represents group mean while the confidence band represents the inter-subject SD. For a given level of gradient moment nulling, σ_ϕ was consistent between slices and timepoints. M_1 and $M_1 + M_2$ have reduced temporal phase variation compared to M_0.

Figure S3. Experiment-1 temporal phase SD. Net mean temporal phase SD averaged across all volunteers for $b = 0$, G_x, and G_y for the three gradient moment nulling levels for a central brain slice. The solid line represents group mean while the confidence band represents the inter-subject SD. The scale of temporal phase variation for G_x and G_y were less than what was observed along G_z (Figure 2). For $b = 0$, temporal phase SD increased with increasing the order of gradient moment nulling. Variation in temporal phase SD between volunteers was reduced with $M_1 + M_2$ gradient moment nulling compared to M_0 for G_x and G_y. For this slice, the average temporal phase SD was similar between levels of gradient moment nulling. A reference bSSFP image of the slice is provided top left.

Figure S4. Net mean $\mu_{||\phi||}$ plotted for all the volunteers in red with the paired attenuation ratio (α) in blue for diffusion encoding along G_z for different slices. Each row corresponds to the slice visualized in the bSSFP image to the left while the confidence band represents the inter-subject SD. Spatial phase gradient varies between slices for a given gradient moment nulling level, as slices closer to the brainstem have higher $\mu_{||\phi||}$ compared to upper cortex slices. TD_0 also had a higher spatial phase on average compared to latter timepoints. This high spatial gradient was typically reduced with M_1 gradient moment nulling. $M_1 + M_2$ across slices was less effective at reducing $\mu_{||\phi||}$ than M_1 as spatial phase gradients trended higher, resulting in a lower attenuation ratio.

Figure S5. Net mean $\mu_{||\phi||}$ plotted for all the volunteers (in red) with the paired attenuation ratio (α) in blue for diffusion encoding along $b = 0$, G_x, and G_y for a central brain slice. $\mu_{||\phi||}$ trends higher with M_1 and $M_1 + M_2$ gradient moment nulling. $b = 0$ has the smallest spatial gradients. These spatial phase gradient increases resulted in lower attenuation ratios for M_1 and $M_1 + M_2$ compared to M_0. A reference bSSFP image of the slice is provided top left.

Figure S6. Experiment-2 temporal phase SD. Net mean temporal phase SD (σ_ϕ) of different slices for G_z diffusion-encoding. Each row corresponds to the slice visualized in the bSSFP image to the left. For a given level of gradient moment nulling, the temporal phase SD was consistent between slices. Light dots indicated the average for a single volunteer while the solid dot and error bar indicated group mean and SD. M_1 and $M_1 + M_2$ have reduced temporal phase variation compared to M_0. The decrease from M_0 to $M_1 + M_2$ was sometimes statistically significant. Stars indicated significance level (* = $p < 0.05$,** = $p < 0.01$).

Figure S7. Experiment-2 temporal phase SD. Net mean temporal phase SD averaged across all volunteers for $b = 0$, G_x, and G_y for the three gradient moment nulling levels for a central brain slice. Light dots indicated the average for a single volunteer while the solid dot and error bar indicated

group mean and SD. For $b = 0$, temporal phase SD trends, temporal phase SD increased with increasing the gradient moment nulling level. Temporal phase SD between volunteers was in some cases reduced with $M_1 + M_2$ gradient moment nulling compared to M_0 for G_x and G_y. The confidence interval of the temporal phase SD ($d\sigma_\phi$) was consistent between levels of gradient moment nulling for G_x and G_y. Significant differences indicated by stars (* $=p < 0.05$, ** $= p < 0.01$). A reference bSSFP image of the slice is provided top left.

Figure S8. Experiment-2 spatial phase gradient. (A) Net mean spatial Phase Gradient ($\mu_{||\phi||}$) (in red) and signal attenuation ratio (α) (in blue) of different slices for G_z diffusion-encoding. Light dots indicated the average for a single volunteer while the solid dot and error bar indicated group mean and SD. Each row corresponds to population data from the slice visualized in the bSSFP image to the left. Signal attenuation ratio trended opposite of spatial phase gradients as reductions in spatial phase gradients lead to higher signal attenuation ratio and subsequently less signal lost. There was a slice-position dependence, as slices closer to the brainstem have higher spatial phase gradients than slices in the upper cortex. The spatial phase gradient for M_1 trended lower than M_0 and was for some slices significant. $M_1 + M_2$ tended to be significantly greater than M_0. (B) The 95% CI of the spatial phase gradient maps ($d\mu_{||\phi||}$) was very similar between levels of gradient moment nulling. There were some instances of significant reduction and some instances of significant increase in $d\sigma_{||\phi||}$ from M_0 to M_1 or from M_0 to $M_1 + M_2$. Significant differences indicated by stars (* $= p < 0.05$, ** $= p < 0.01$).

Figure S9. Experiment-2 spatial phase gradient. (A) Net mean spatial Phase Gradient ($\mu_{||\phi||}$) (in red) and signal attenuation ratio (α) (in blue) for a central brain slice and $b = 0$, G_x, and G_y diffusion-encoding. Light dots indicated the average for a single volunteer while the solid dot and error bar indicated group mean and SD. The resultant signal attenuation ratio (α) is plotted in blue. For $b = 0$, spatial phase gradient increased with increasing gradient moment nulling. Spatial phase gradient between volunteers was in some cases reduced with M_1 gradient moment nulling compared to M_0 for G_x and G_y; however, there were also cases with a significant increase from M_0 to M_1 or $M_1 + M_2$. Signal attenuation has inverse trends in which spatial phase gradient increases result in a smaller ratio, indicating more attenuation. (B) The 95% CI of the spatial phase gradient maps ($d\mu_{||\phi||}$) was generally consistent between levels of gradient moment nulling for G_x and G_y. Significant differences indicated by stars (* $= p < 0.05$, ** $= p < 0.01$). A reference bSSFP image of the slice is provided top left.

Figure S10. Experiment-3 temporal phase SD. Net average temporal phase SD (σ_ϕ) for $b = 0$, G_x, G_y, and G_z for the basal, mid-ventricular, and apical slices. Each row corresponds to the slice visualized in the bSSFP image to the left. Light dots indicated the average for a single volunteer while the solid dot and error bar indicated group mean and SD. Temporal phase SD was not significantly reduced from M_0 to M_1. For G_x, G_y, and G_z, $M_1 + M_2$ significantly (at least $p < 0.05$) reduced temporal phase SD in comparison to M_0 and M_1. For $b = 0$, no significant differences between temporal phase SD of different levels of moment nulling were detected. Significance indicated by stars (* $= p < 0.05$, ** $= p < 0.01$, *** $= p < 0.001$).

Figure S11. Experiment-3 spatial phase gradient. Net average spatial phase gradient ($\mu_{||\phi||}$) (in red) and average signal attenuation ratio (α) (in blue) for $b = 0$, G_x, G_y, and G_z for the basal, mid-ventricular, and apical slices. Each row corresponds to the slice visualized in the bSSFP image to the left. Light dots indicated the average for a single volunteer while the solid dot and error bar indicated group mean and SD. With diffusion-encoding, M_1 and $M_1 + M_2$ gradient moment nulling had significantly lower the temporal phase SD. $M_1 + M_2$ average spatial phase gradient was significantly lower than M_1. Significance indicated by stars (* $= p < 0.05$, ** $= p < 0.01$, *** $= p < 0.001$).

How to cite this article: Hannum AJ, Cork TE, Setsompop K, Ennis DB. Phase stabilization with motion compensated diffusion weighted imaging. *Magn Reson Med*. 2024;1-16. doi: 10.1002/mrm.30218